ADVANCED MATERIALS
www.advmat.de

Molybdenum-Enriched $Mo_{0.5}Ru_{0.5}O_2$ Nanoparticles for Efficient and Stable Oxygen Evolution Reaction

Kaizhu Zeng, In Gyeom Kim, Fangyuan Liu, Peiyuan Gao, Litao Yan, Bhuvana Modachur Sivakumar, Thomas W Wietsma, Yiheng Du, Qian Zhang, Chong Yang, Yang Hu, Tangyuan Li, Shu Hu, Yuyan Shao, and Liangbing Hu**

Ruthenium dioxide (RuO_2) shows excellent activity toward the acidic oxygen evolution reaction (OER); however, its practical application is limited by poor long-term stability. Herein, a single-phase $Mo_{0.5}Ru_{0.5}O_2$ nanoparticle catalyst is reported with a high Mo content, synthesized via high-temperature thermal shock treatment under an oxygen atmosphere (HTSO), exhibiting high activity and stability in OER. The HTSO technique involves rapidly heating the precursor to ≈1200 °C for ≈0.05 s in oxygen, followed by immediate quenching at a rate of ≈10^4 °C s^{-1}. The resulting nanoparticles exhibit a uniform size of ≈10 nm and homogeneous elemental mixing, overcoming the thermodynamic barriers that typically lead to phase separation in conventional synthesis methods. The $Mo_{0.5}Ru_{0.5}O_2$ catalyst achieves an overpotential of 210 mV at 10 mA cm^{-2} and maintains stable performance over 300 h at 50 mA cm^{-2} in OER, significantly surpassing the stability of RuO_2 and other reported high-metal-content doped RuO_2 catalysts. High-valence Mo, with its multiple accessible oxidation states and compatible ionic radius, serves as an ideal dopant for RuO_2, enabling stable lattice substitution, effective electron donation, and ultimately suppressing Ru over-oxidation while enhancing stability. This approach enhances catalyst stability and Ru utilization, providing a versatile platform for synthesizing other metal-doped RuO_2 systems toward cost-effective and stable OER catalysts.

1. Introduction

The oxygen evolution reaction (OER) in acidic media is a crucial yet challenging process for proton-exchange membrane water electrolyzers.[1–3] Noble metal oxides, such as ruthenium dioxide (RuO_2) and iridium dioxide (IrO_2), are the state-of-the-art catalysts in these harsh conditions because common transition metals rapidly corrode.[4–6] Among them, RuO_2, which is at least five times less expensive than IrO_2, is widely regarded as a benchmark OER catalyst in acid due to its exceptional intrinsic activity.[7–12] However, the practical deployment of RuO_2 is severely limited by its poor long-term stability under harsh conditions. During OER, Ru can undergo over-oxidation to higher valence states and dissolve into the electrolyte, leading to catalyst deactivation.[10,11] This well-known activity-stability tradeoff motivates the development of "modified Ru-based catalysts" that retain high OER activity while improving stability in acidic environments.[12–14]

K. Zeng, F. Liu, Y. Du, Q. Zhang, C. Yang, T. Li, L. Hu
Department of Electrical and Computer Engineering
Yale University
New Haven, CT 06511, USA
E-mail: liangbing.hu@yale.edu

I. G. Kim, L. Yan, B. M. Sivakumar, T. W Wietsma, Y. Shao
Energy and Environment Directorate
Pacific Northwest National Laboratory
3335 Innovation Blvd., Richland, WA 99354, USA
E-mail: litao.yan@pnnl.gov

P. Gao
Physical and Computational Sciences Directorate
Pacific Northwest National Laboratory
3335 Innovation Blvd., Richland, WA 99354, USA

Y. Hu, S. Hu
Department of Chemical and Environmental Engineering
Yale University
New Haven, CT 06520, USA

S. Hu
Energy Sciences Institute
Yale West Campus
West Haven, CT 06516, USA

S. Hu, L. Hu
Center for Materials Innovation
Yale University
New Haven, CT 06511, USA

L. Hu
Department of Materials Science
Yale University
New Haven, CT 06511, USA

The ORCID identification number(s) for the author(s) of this article can be found under https://doi.org/10.1002/adma.202520210

DOI: 10.1002/adma.202520210

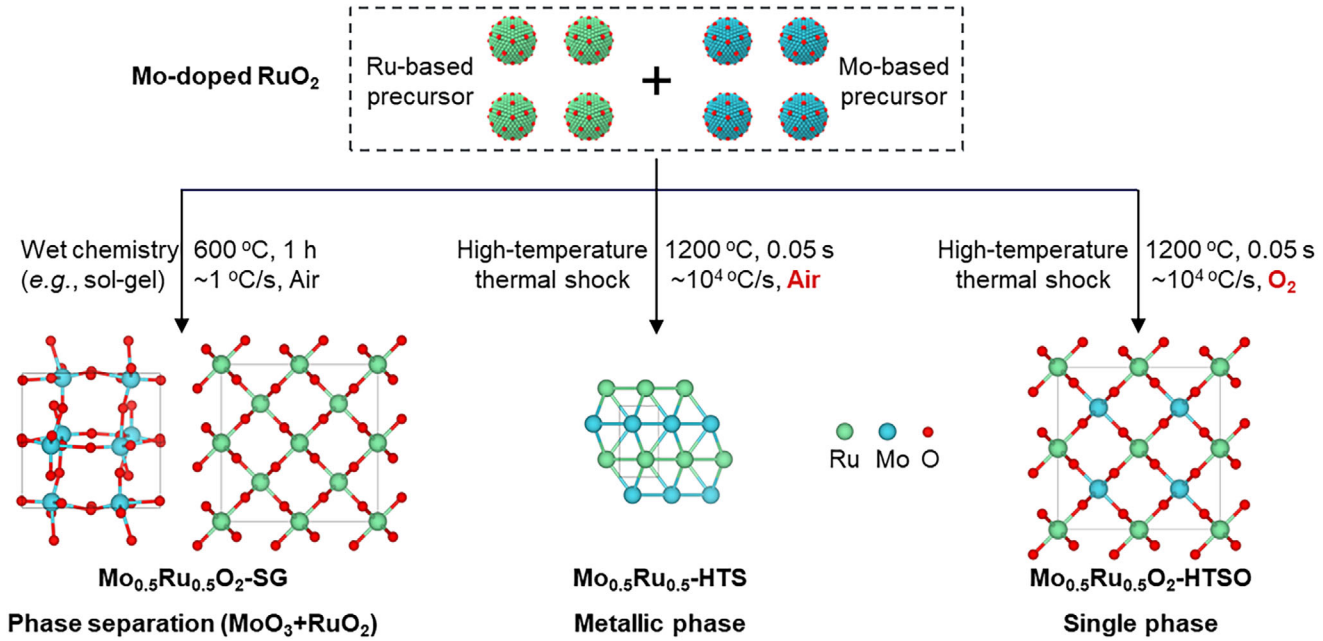

Figure 1. Schematic illustration of $Mo_{0.5}Ru_{0.5}O_2$ nanoparticles synthesized by sol–gel and high-temperature thermal shock methods. The $Mo_{0.5}Ru_{0.5}O_2$-SG sample prepared via the sol–gel (SG) method exhibits phase separation (MoO_3 and RuO_2), and the $Mo_{0.5}Ru_{0.5}$-HTS sample synthesized by the high-temperature thermal shock method under an air atmosphere (HTS) shows metallic phase. In contrast, the $Mo_{0.5}Ru_{0.5}O_2$-HTSO sample synthesized by the high-temperature thermal shock method under an oxygen atmosphere (HTSO) exhibits a single-phase oxide structure with high catalytic activity and stability toward the oxygen evolution reaction (OER).

One promising approach to enhance the stability and reduce the cost of Ru-based catalysts is heteroatom doping, involving partially substituting Ru with a less expensive, more abundant element.[15] Among various dopants, molybdenum (Mo) has attracted attention for tuning RuO_2 because of its multivalent nature and strong affinity.[16–21] It is expected to more effectively suppress Ru over-oxidation by increasing the electron density and enhancing lattice stability under harsh OER conditions. Furthermore, the higher dopant content may reduce the risk of structural collapse by minimizing dopant leaching and promoting uniform charge distribution within the RuO_2 framework. Despite the promising potential of Mo doping, synthesizing a single-phase Ru-Mo oxide nanoparticle at high Mo contents (e.g., 50 at%) remains a significant challenge.

RuO_2 has a tetragonal crystal structure,[22] whereas the most stable form of molybdenum oxide under ambient conditions is MoO_3 (orthorhombic) or MoO_2 (monoclinic), significantly different structures.[23] Thermodynamically, a homogeneous $Mo_xRu_{1-x}O_2$ (x represents a doping content of Mo) tetragonal phase is not favored; instead, the components tend to segregate into their own oxide phases (RuO_2 and MoO_3/MoO_2). High-temperature heating (900 °C for 72 h) followed by rapid quenching has been employed to synthesize $Mo_xRu_{1-x}O_2$ ($0.0 \leq x \leq 0.5$) ceramic pellets, effectively overcoming thermodynamic barriers to achieve a single-phase structure.[24] This prolonged annealing facilitates particle sintering, leading to the formation of bulk materials. To reduce these bulk materials to the nanoscale for catalytic applications, wet-chemical methods such as hydrothermal synthesis have been explored. However, at higher Mo contents, these techniques often lead to phase separation or the formation of heterogeneous structures, rather than achieving a solid-solution structure.[25,26] These limitations of traditional synthesis have, to date, restricted most reported Mo-Ru oxide nanoparticles to either low Mo doping levels (where a solid solution can be maintained) or composite structures (RuO_2 supported on MoO_3, etc.), rather than a single-phase material.

In this work, we overcome these synthesis challenges by employing high-temperature thermal shock synthesis[27,28] under an oxygen atmosphere (HTSO) to produce single-phase $Mo_xRu_{1-x}O_2$ ($0.0 \leq x \leq 0.5$) nanoparticles with a record-high Mo content of $x = 0.5$ (**Figure 1**). The thermal shock technique involves rapidly heating the precursor to an ultrahigh temperature (≈1200 °C) for an extremely short duration (≈0.05 s) in oxygen, followed by immediate rapid quenching (cooling rates on the order of 10^4 °C s^{-1}). This nonequilibrium approach contrasts sharply with conventional slow annealing. A brief high-temperature exposure in oxygen facilitates intimate atomic intermixing of Mo and Ru, leading to crystallization into a single tetragonal phase. A subsequent rapid quench under controlled temperature and oxygen atmosphere preserves the mixed structure by preventing phase separation and elemental segregation. As a result, $Mo_{0.5}Ru_{0.5}O_2$ with a uniform size of ≈10 nm is realized as a single-phase oxide nanoparticle, a composition that is virtually inaccessible via standard calcination, wet chemistry methods like sol–gel (SG), or high-temperature thermal shock under an air atmosphere (HTS, Figure 1). Our developed $Mo_{0.5}Ru_{0.5}O_2$ catalyst not only preserves the high oxygen evolution reaction (OER) activity and Ru utilization, but also exhibits remarkably enhanced durability. In acidic OER testing, the $Mo_{0.5}Ru_{0.5}O_2$ catalyst shows an overpotential of 210 mV at a current density of 10 mA cm^{-2} and maintains stable performance for over 300 h at 50 mA cm^{-2}, far surpassing the stability of $Mo_{0.2}Ru_{0.8}O_2$ and RuO_2 catalysts. Compared to

state-of-the-art OER catalysts, the $Mo_{0.5}Ru_{0.5}O_2$ catalyst with reduced Ru content ranks among the most stable. The enhanced stability of $Mo_{0.5}Ru_{0.5}O_2$ arises from the ability of high-valence Mo, with its accessible oxidation states and compatible ionic radius, to substitute stably into the RuO_2 lattice, donate electrons to Ru, and thereby suppress over-oxidation and improve OER stability. Notably, the heavily doped $Mo_{0.5}Ru_{0.5}O_2$ catalyst demonstrates significantly improved stability compared to conventional low-doped counterparts, highlighting the critical role of increased dopant concentration in enhancing catalyst longevity. This HTSO approach is also applicable to other metal-doped RuO_2 systems, enabling the synthesis of higher metal-doped RuO_2 catalysts and offering a pathway for OER performance optimization.

2. Results and Discussion

$Mo_xRu_{1-x}O_2$ nanoparticles (x = 0.0, 0.2, 0.5, 0.6, 1.0) were synthesized via a high-temperature thermal shock method under an oxygen atmosphere (HTSO) on commercial carbon paper substrates (**Figure 2a**; Figure S1, Supporting Information; see Experimental Section for details). A range of temperature profiles and atmospheric conditions was systematically explored to optimize the formation of a single-phase solid solution of $Mo_xRu_{1-x}O_2$. The optimal synthesis condition was achieved in an oxygen atmosphere with a temperature profile of 1200 °C for 0.05 s, as confirmed by the infrared temperature image during Joule heating of the precursor-loaded carbon paper (Figure 2b). Under these conditions, uniform $Mo_{0.5}Ru_{0.5}O_2$-HTSO nanoparticles were successfully obtained, as shown in the scanning electron microscopy (SEM) images (Figure 2c,d; Figure S2, Supporting Information). The nanoparticles exhibited an average size of ≈10 nm (Figure S3, Supporting Information), uniformly distributed across the carbon paper substrate. Energy-dispersive X-ray spectroscopy (EDS) elemental mapping of the $Mo_{0.5}Ru_{0.5}O_2$-HTSO sample (Figure 2e) revealed a homogeneous distribution of Mo, Ru, and O within individual nanoparticles. This uniform elemental distribution confirms the formation of a nanoscale solid solution, rather than a physical mixture of separate oxide phases.

Atomic-resolution high-angle annular dark-field scanning transmission electron microscopy (HAADF-STEM) of $Mo_{0.5}Ru_{0.5}O_2$-HTSO (Figure 2f) revealed clear lattice fringes with measured d-spacings of 2.29 Å for the (200) planes and 2.61 Å for the ($\bar{1}$01) planes, consistent with the tetragonal structure of RuO_2. Inductively coupled plasma (ICP) analysis (Figure S4, Supporting Information) confirmed that the atomic ratio of Ru to Mo in the $Mo_{0.5}Ru_{0.5}O_2$-HTSO sample closely matched the intended composition. X-ray diffraction (XRD) analysis (Figure 2g-IV) also confirmed the single-phase tetragonal structure of $Mo_{0.5}Ru_{0.5}O_2$-HTSO, showing a set of diffraction peaks that closely match those of RuO_2 (Crystallography Open Database, COD: 96-100-0059). Prominent diffraction peaks at 28.0° and 35.1° corresponding to the (110) and (101) planes were observed, while signals at 25.9° and 54.5° were attributed to the carbon paper substrate (Figure S5, Supporting Information).

Synthesizing single-phase $Mo_{0.5}Ru_{0.5}O_2$ nanoparticles with high molybdenum (Mo) content is challenging due to thermodynamic constraints. To address this, various synthesis methods, atmospheric conditions, and heating temperatures were explored to achieve single-phase $Mo_{0.5}Ru_{0.5}O_2$. A sol–gel (SG) method coupled with furnace heating (600 °C for 1 h in air) followed by slow quenching (≈1 °C s^{-1}) was employed to synthesize $Mo_xRu_{1-x}O_2$ (x = 0.2 and 0.5). XRD patterns revealed that $Mo_{0.2}Ru_{0.8}O_2$-SG exhibited a single-phase structure, as indicated by diffraction peaks similar to those of RuO_2 (Figure S6, Supporting Information). In contrast, $Mo_{0.5}Ru_{0.5}O_2$-SG showed phase separation, with distinct peaks corresponding to MoO_3 (COD: 96-153-7655, Figure 2g-I).[29] The low-temperature heating at 600 °C does not provide sufficient energy to promote homogeneous mixing of Ru and Mo, and the slow quenching rate (≈1 °C s^{-1}) allows Mo to crystallize as a separate phase (Figure 2h). The presence of an oxygen atmosphere during shock treatment is crucial for fully oxidizing Ru and Mo and stabilizing them within the lattice during synthesis. Using air as the synthesis atmosphere did not yield single-phase $Mo_{0.5}Ru_{0.5}O_2$, but instead resulted in the formation of a Ru-based metallic phase, as revealed by its XRD patterns (COD: 96-810-4269, Figure 2g-II). Excess oxygen likely suppresses the reduction of oxidized Ru, decreasing the Gibbs free energy of formation of this oxide system[30] and favoring the solid solution of $Mo_{0.5}Ru_{0.5}O_2$ (Figure 2i). A proper temperature (e.g., 1200 °C) is also necessary for the single-phase $Mo_{0.5}Ru_{0.5}O_2$ formation. XRD of $Mo_{0.5}Ru_{0.5}O_2$ synthesized at 900 °C showed no distinct peaks (Figure S7, Supporting Information), while synthesis at 1500 °C resulted in a mixture of metallic Ru-based and oxide RuO_2-based phases (Figure 2g-III). Excessive temperatures may induce the reduction of the noble metal Ru due to its low oxidation potential. As illustrated by the Ellingham diagram (Figure 2j), elevated temperatures thermodynamically favor the reduction of metal oxides, which can result in phase separation.[30] Based on these optimization strategies, we attribute the successful synthesis of single-phase $Mo_xRu_{1-x}O_2$ ($0.0 \leq x \leq 0.5$, Figure 2k; Figure S8, Supporting Information) to the HTSO method: the oxygen-rich, high-temperature environment drives Ru and Mo atoms into a single structure before significant phase segregation can occur, and rapid quenching kinetically traps the mixed-oxide structure, preventing nanoparticle growth and sintering. Essentially, the material does not have the opportunity to "de-mix" into Ru- and Mo-rich domains, in stark contrast to the prolonged annealing and slow quenching in traditional syntheses. The HTSO method is universal for synthesizing metal-doped RuO_2 (Figure S9 and Table S1, Supporting Information) and could potentially be industrialized using conventional conveyor-belt furnaces with only minor modifications, such as increasing the conveyor speed and reducing the heating zone length, to control the heating duration (Figure S10, Supporting Information).

To highlight the effectiveness of the HTSO synthesis method in forming single-phase $Mo_{0.5}Ru_{0.5}O_2$-HTSO, its OER performance was compared with that of $Mo_{0.5}Ru_{0.5}O_2$-SG prepared via a conventional sol–gel method. The OER performances of RuO_2-HTSO, $Mo_{0.2}Ru_{0.8}O_2$-HTSO, $Mo_{0.5}Ru_{0.5}O_2$-HTSO, and $Mo_{0.5}Ru_{0.5}O_2$-SG were evaluated using a three-electrode system in O_2-saturated 0.1 M $HClO_4$ electrolyte, with a graphite counter electrode and an Ag/AgCl reference electrode. Linear sweep voltammetry (LSV) tests were conducted under acidic conditions (**Figure 3a**). Introducing 20 at% Mo into the RuO_2 structure via the HTSO method significantly improved OER performance compared to pure RuO_2. Increasing the Mo doping to 50 at% led to a slight decrease in activity, as indicated by the current

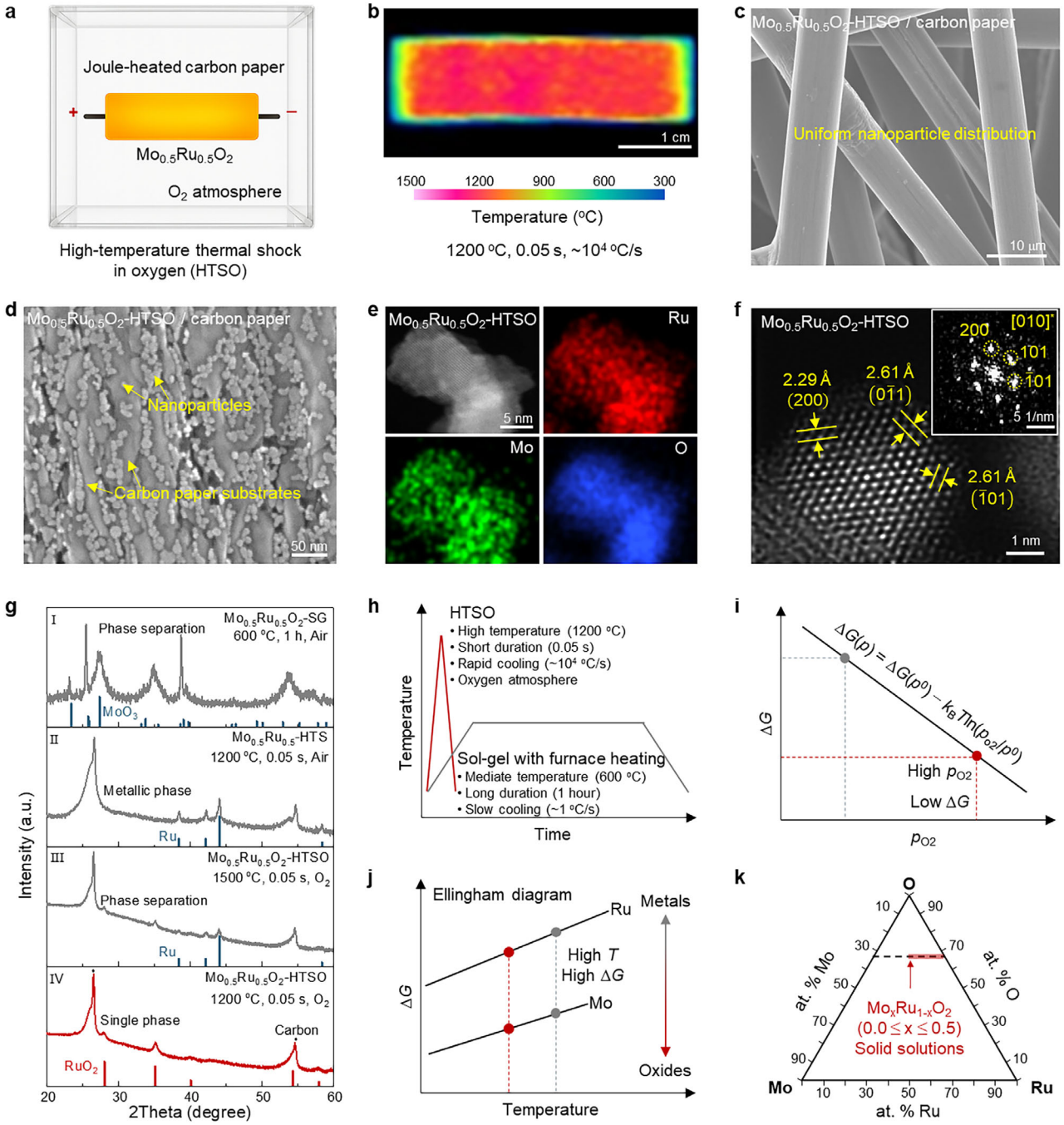

Figure 2. Synthesis and characterization of $Mo_{0.5}Ru_{0.5}O_2$ nanoparticles. a) Schematic illustration of the synthesis of $Mo_{0.5}Ru_{0.5}O_2$ via high-temperature thermal shock under an oxygen atmosphere (HTSO); b) Infrared (IR) image of Joule-heated $Mo_{0.5}Ru_{0.5}O_2$ on carbon paper; The thermal profile reaches 1200 °C for 0.05 s in oxygen: c,d) SEM images of $Mo_{0.5}Ru_{0.5}O_2$ on carbon paper synthesized by HTSO; e) TEM elemental maps of Mo, Ru, and O in $Mo_{0.5}Ru_{0.5}O_2$-HTSO; f) Atomic-resolution structure and corresponding fast Fourier transform (FFT) pattern of $Mo_{0.5}Ru_{0.5}O_2$-HTSO; g) XRD patterns of $Mo_{0.5}Ru_{0.5}O_2$ synthesized under various conditions: (I) sol–gel (SG), (II) HTS at 1200 °C for 0.05 s in air, (III) HTSO at 1500 °C for 0.05 s in oxygen, and (IV) HTSO at 1200 °C for 0.05 s in oxygen; h) Schematic comparison of synthesis temperature and duration for HTSO and SG with furnace heating. HTSO enables short-time heating and rapid cooling, facilitating the formation of single-phase $Mo_{0.5}Ru_{0.5}O_2$. In contrast, SG with furnace heating involves prolonged heating and slow cooling, which promotes phase separation; i) Schematics showing Gibbs free energy change for oxide formation as a function of oxygen partial pressure (P_{O2}). At a given temperature, Gibbs free energy decreases with increasing P_{O2}, indicating greater oxide stability at higher oxygen partial pressures; j) Schematic of the formation Gibbs free energies of Ru- and Mo-based oxides as a function of temperature (Ellingham diagram). At high temperatures, both Ru- and Mo-based oxides tend to reduce to their respective metals. Compared to Ru, Mo has a higher oxidation potential, making it more easily oxidized; k) Phase diagram of $Mo_xRu_{1-x}O_2$ ($0.0 \le x \le 0.5$), showing a single-phase solid-solution structure within the studied composition range.

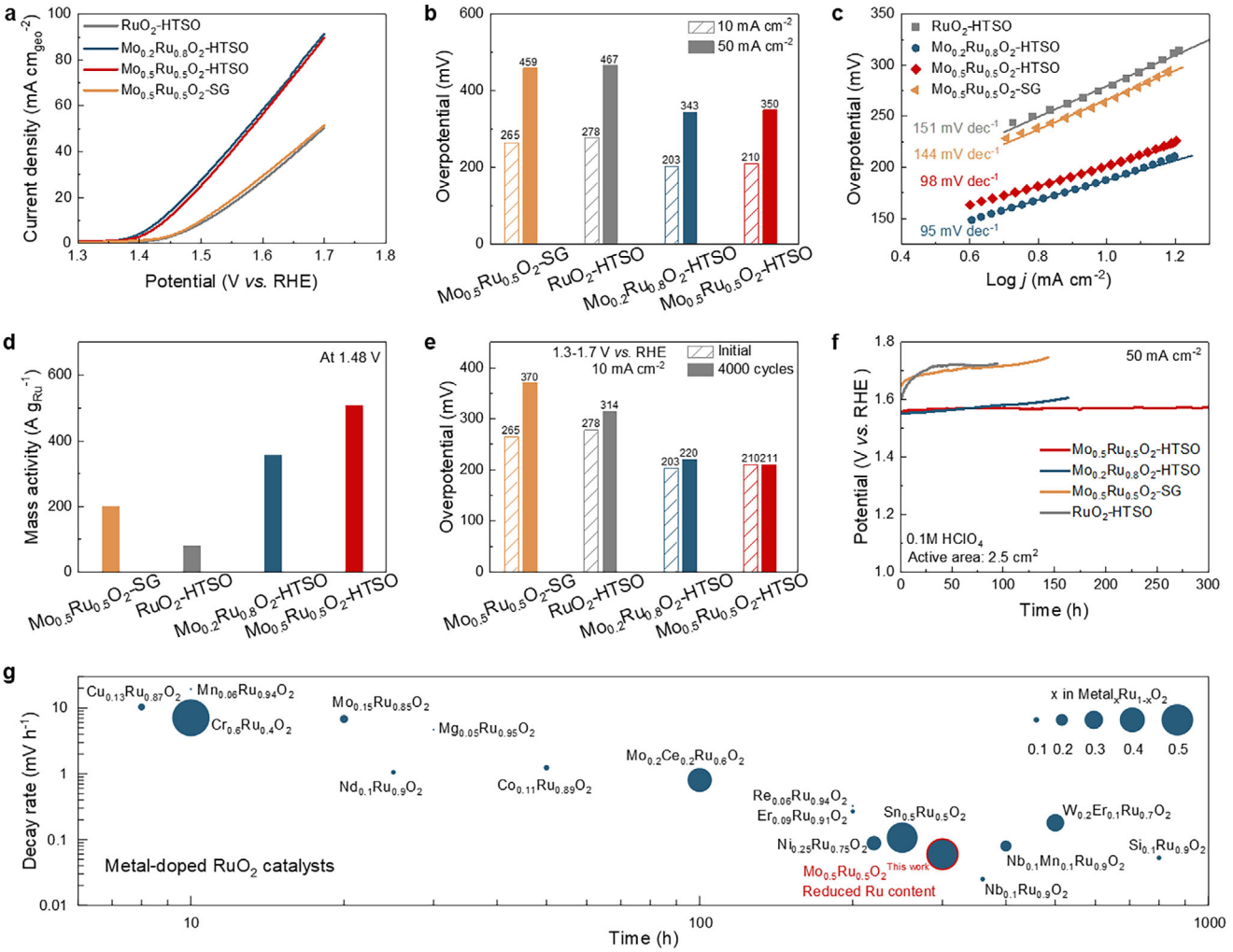

Figure 3. OER activity and stability of $Mo_{0.5}Ru_{0.5}O_2$. a–d): a) Polarization curves, b) overpotentials at 10 mA cm^{-2} and 50 mA cm^{-2}, c) corresponding Tafel plots, and d) mass activities of RuO_2-HTSO, $Mo_{0.2}Ru_{0.8}O_2$-HTSO, $Mo_{0.5}Ru_{0.5}O_2$-HTSO, and $Mo_{0.5}Ru_{0.5}O_2$-SG; e) Changes in overpotentials before and after 4000 CV cycles for RuO_2-HTSO, $Mo_{0.2}Ru_{0.8}O_2$-HTSO, $Mo_{0.5}Ru_{0.5}O_2$-HTSO, and $Mo_{0.5}Ru_{0.5}O_2$-SG; f) Chronopotentiometry (CP) tests at 50 mA cm^{-2} for RuO_2-HTSO, $Mo_{0.2}Ru_{0.8}O_2$-HTSO, $Mo_{0.5}Ru_{0.5}O_2$-HTSO, and $Mo_{0.5}Ru_{0.5}O_2$-SG; g) Comparison of the decay rate (mV h^{-1}) between $Mo_{0.5}Ru_{0.5}O_2$-HTSO and reported metal-doped RuO_2 catalysts.

density. In contrast, MoO_3-HTSO shows negligible activity, confirming that the primary active sites originate from Ru (Figure S11, Supporting Information). The overpotentials for $Mo_{0.5}Ru_{0.5}O_2$-HTSO are 210 mV at 10 mA cm^{-2} and 350 mV at 50 mA cm^{-2}, which are similar to those of $Mo_{0.2}Ru_{0.8}O_2$-HTSO (Figure 3b). The electrochemically active surface area-related performance of $Mo_{0.5}Ru_{0.5}O_2$-HTSO also demonstrates its higher intrinsic activity (Figures S12 and S13, Supporting Information). However, $Mo_{0.5}Ru_{0.5}O_2$-SG exhibited lower OER activity than $Mo_{0.5}Ru_{0.5}O_2$-HTSO. When comparing $Mo_{0.2}Ru_{0.8}O_2$-SG and $Mo_{0.5}Ru_{0.5}O_2$-SG, the latter demonstrated poorer OER performance (Figure S14, Supporting Information). This low activity is attributed to the existence of inactive MoO_3, which is revealed by the XRD results (Figure 2g-I). These findings highlight the superiority of the HTSO method for synthesizing single-phase $Mo_{0.5}Ru_{0.5}O_2$ as an effective OER catalyst.

Tafel slopes were calculated to evaluate the OER kinetics of the studied catalysts. $Mo_{0.2}Ru_{0.8}O_2$-HTSO and $Mo_{0.5}Ru_{0.5}O_2$-HTSO exhibited similarly low Tafel slopes of 95.1 and 98.4 mV dec^{-1}, respectively (Figure 3c), indicating comparable OER kinetics.[31,32] In contrast, $Mo_{0.5}Ru_{0.5}O_2$-SG, which contains the MoO_3 phase, exhibited a relatively high Tafel slope of 144.2 mV dec^{-1}. This behavior is attributed to the presence of MoO_3, which displays negligible OER activity (Figure S11, Supporting Information). Notably, the mass activity of $Mo_{0.5}Ru_{0.5}O_2$-HTSO at an overpotential of 250 mV was 1.4, 4.0, and 6.5 times higher than that of $Mo_{0.2}Ru_{0.8}O_2$-HTSO, $Mo_{0.5}Ru_{0.5}O_2$-SG, and RuO_2-HTSO, respectively (Figure 3d), indicating a higher Ru utilization efficiency toward the OER. In addition, comparison of turnover frequencies (TOF)[33] at an overpotential of 250 mV revealed significant differences. The TOF of $Mo_{0.5}Ru_{0.5}O_2$-HTSO was 0.133 s^{-1}, higher than $Mo_{0.2}Ru_{0.8}O_2$-HTSO (0.09 s^{-1}) and much higher than $Mo_{0.5}Ru_{0.5}O_2$-SG (0.033 s^{-1}) (Figure S15, Supporting Information). Electrochemical impedance spectroscopy (EIS) results (Figure S16, Supporting Information) showed that $Mo_{0.2}Ru_{0.8}O_2$-HTSO and $Mo_{0.5}Ru_{0.5}O_2$-HTSO exhibited similarly low charge

transfer resistance, suggesting enhanced OER kinetics compared to $Mo_{0.5}Ru_{0.5}O_2$-SG and RuO_2-HTSO.[11,31,32] Therefore, $Mo_{0.5}Ru_{0.5}O_2$-HTSO with high Mo doping exhibited the best electrochemical performance, which can be attributed to the following reasons: The HTSO process enables the formation of a homogeneous RuO_2-based phase even at high Mo doping levels, whereas the conventional sol–gel method fails to do so; and high Mo doping promotes the formation of more low-valence Ru^{3+} species, as revealed by cycling voltammogram (CV, Figure S17, Supporting Information), X-ray photoelectron spectroscopy (XPS, Figure S18 and Tables S2 and S3, Supporting Information), and density of states (DOS) (Figures S19, Supporting Information) analyses.

Beyond intrinsic activity, stability is a critical parameter for acidic OER electrocatalysts operating at high current densities. The stability of $Mo_{0.5}Ru_{0.5}O_2$-HTSO was comprehensively evaluated using cycling voltammogram (CV), chronoamperometry (CA), and chronopotentiometry (CP) tests. Accelerated stability tests (ADTs) involved 4000 CV cycles between 1.3–1.7 V_{RHE} at a sweep rate of 50 mV s^{-1} in 0.1 M $HClO_4$ under Ar purging. Linear sweep voltammetry (Figure S20, Supporting Information) showed that $Mo_{0.5}Ru_{0.5}O_2$-HTSO exhibited minimal degradation, with only a 1.0 mV increase relative to the initial overpotential at 10 mA cm^{-2}, whereas $Mo_{0.2}Ru_{0.8}O_2$-HTSO showed a larger decay of 17 mV increase (Figure 3e), indicating that higher Mo doping effectively mitigates OER degradation. In contrast, $Mo_{0.5}Ru_{0.5}O_2$-SG showed a substantial 105 mV increase in overpotential at 10 mA cm^{-2}, likely due to MoO_3 dissolution and subsequent structural collapse under acidic OER conditions. Furthermore, inductively coupled plasma mass spectrometry (ICP-MS) was conducted to analyze the concentration of dissolved Ru in the electrolyte after a 24-h CA stability test at 1.65 V_{RHE} (Figure S21, Supporting Information). The ICP-MS results revealed that the Ru ion concentration from $Mo_{0.5}Ru_{0.5}O_2$-HTSO was significantly lower than that from $Mo_{0.2}Ru_{0.8}O_2$-HTSO, indicating that the higher Mo doping level and the formation of a stable single-phase structure in $Mo_{0.5}Ru_{0.5}O_2$ contribute to its improved OER activity and durability.

The stability of the catalysts was evaluated using CP at a current density of 50 mA cm^{-2}. $Mo_{0.5}Ru_{0.5}O_2$-HTSO exhibited no significant voltage decay over 300 h, whereas $Mo_{0.2}Ru_{0.8}O_2$-HTSO showed a decay of more than 50 mV after just 50 h (Figure 3f). In contrast, $Mo_{0.5}Ru_{0.5}O_2$-SG and RuO_2-HTSO exhibited voltage decays of 100 and 123 mV after 140 and 90 h, respectively. These results highlight the superior stability of $Mo_{0.5}Ru_{0.5}O_2$-HTSO, attributed to its single-phase structure achieved via the HTSO method. Using voltage decay per hour as a figure of merit, we compared $Mo_{0.5}Ru_{0.5}O_2$-HTSO with other reported metal-doped RuO_2 catalysts (Figure 3g; Table S4, Supporting Information).[11,16,31–47] $Mo_{0.5}Ru_{0.5}O_2$-HTSO exhibited excellent stability with a voltage decay rate of only 0.06 mV h^{-1}, despite its significantly reduced Ru content, underscoring its cost-effectiveness and practical applicability.

To explore the origin of high stability, a series of characterizations, including XRD, TEM, and XPS, were performed for $Mo_{0.5}Ru_{0.5}O_2$-HTSO after 300 h of OER operation at 50 mA cm^{-2} in an acidic electrolyte to investigate its structural evolution. Elemental mapping confirmed that Ru, Mo, and O remained uniformly distributed throughout the sample (**Figure** 4a). The HADDF-STEM image further revealed a well-maintained single-phase tetragonal structure, as evidenced by lattice spacings of 3.24 Å for (1$\bar{1}$0) and 2.61 Å for (1$\bar{0}$1) (Figure 4b). Moreover, the XRD pattern of $Mo_{0.5}Ru_{0.5}O_2$-HTSO after OER testing showed no significant changes, with only weaker peak intensities compared to the pristine sample, likely due to partial surface amorphization (Figure 4c). In contrast, the XRD and XPS results of $Mo_{0.5}Ru_{0.5}O_2$-SG revealed the disappearance of MoO_3-related peaks after testing, suggesting that the unstable MoO_3 phase dissolved under acidic OER conditions (Figures S22 and S23, Supporting Information). The robust stability of $Mo_{0.5}Ru_{0.5}O_2$-HTSO was also confirmed by XPS analysis. For the Ru *3p* spectra, the Ru^{3+}/Ru^{4+} ratio decreased slightly by 4.6% (from 0.87 to 0.83) after the stability test, indicating some oxidation under high anodic potentials (Figure 4d,e).[11,32] In comparison, $Mo_{0.2}Ru_{0.8}O_2$-HTSO and RuO_2-HTSO exhibited much larger reductions in the Ru^{3+}/Ru^{4+} ratio, 13.9% and 35.3%, respectively, highlighting the enhanced structural and chemical stability of the higher Mo-doped sample. The Mo 3*d* spectra before and after OER stability testing reveals that the Mo^{5+} $3d_{5/2}$ and Mo^{5+} $3d_{3/2}$ peaks shift by +0.11 and +0.23 eV, respectively. This positive shift, along with the increase in the Mo^{6+}/Mo^{5+} ratio after the test, indicates that only minor surface oxidation of Mo occurred during the stability test at high anodic potential (Figure 4f; Table S3, Supporting Information).

To understand the stabilization mechanism, density functional theory (DFT) calculations were performed to determine the formation free energy of oxygen vacancies (ΔG_{OV}) in Mo-doped RuO_2 systems (Figure 4g). For $Mo_{0.5}Ru_{0.5}O_2$, the ΔG_{OV} was calculated to be 3.03 eV, higher than those of pure RuO_2 (2.26 eV), $Mo_{0.17}Ru_{0.83}O_2$ (2.66 eV), and $Mo_{0.33}Ru_{0.67}O_2$ (2.84 eV). These results indicate that $Mo_{0.5}Ru_{0.5}O_2$ effectively increases the energy barrier for oxygen vacancy formation, thereby suppressing Ru dissolution under acidic OER conditions.[31] The four-step DFT free energy calculations of the OER via the adsorbate evolution mechanism are presented in Figure 4h. For all designed samples, the rate-determining step (RDS) was identified as the transition between the $^*O$ and $^*OOH$ intermediates, representing the critical bottleneck in the catalytic pathway. The calculated ΔG of the RDS (Figure 4i) for $Mo_{0.5}Ru_{0.5}O_2$ (1.93 eV) is lower than that of pristine RuO_2 (2.08 eV), indicating that Mo doping effectively reduces the energy barrier and thereby enhances the OER catalytic activity.

Building upon the above findings, high-level Mo doping in RuO_2 emerges as a promising strategy to address the intrinsic stability limitations of pristine RuO_2, while also reducing material costs and enhancing intrinsic activity. Although previous studies have demonstrated that metal-doped RuO_2 with doping levels below 20 at% can improve stability, the dopant metals are often susceptible to oxidation and dissolution under prolonged high-potential OER conditions, ultimately leading to structural degradation and collapse of the RuO_2 framework. In contrast, heavy Mo doping within the RuO_2 lattice can significantly reinforce its structural integrity, enabling the framework to remain well structure even after extended OER operation. This structural preservation is believed to be a key factor underlying the observed enhancement in long-term stability (Figure 4j).

Beyond Mo doping, we synthesized $Nb_{0.5}Ru_{0.5}O_2$, $Mn_{0.5}Ru_{0.5}O_2$, $Sn_{0.5}Ru_{0.5}O_2$, and $Ce_{0.5}Ru_{0.5}O_2$ and evaluated

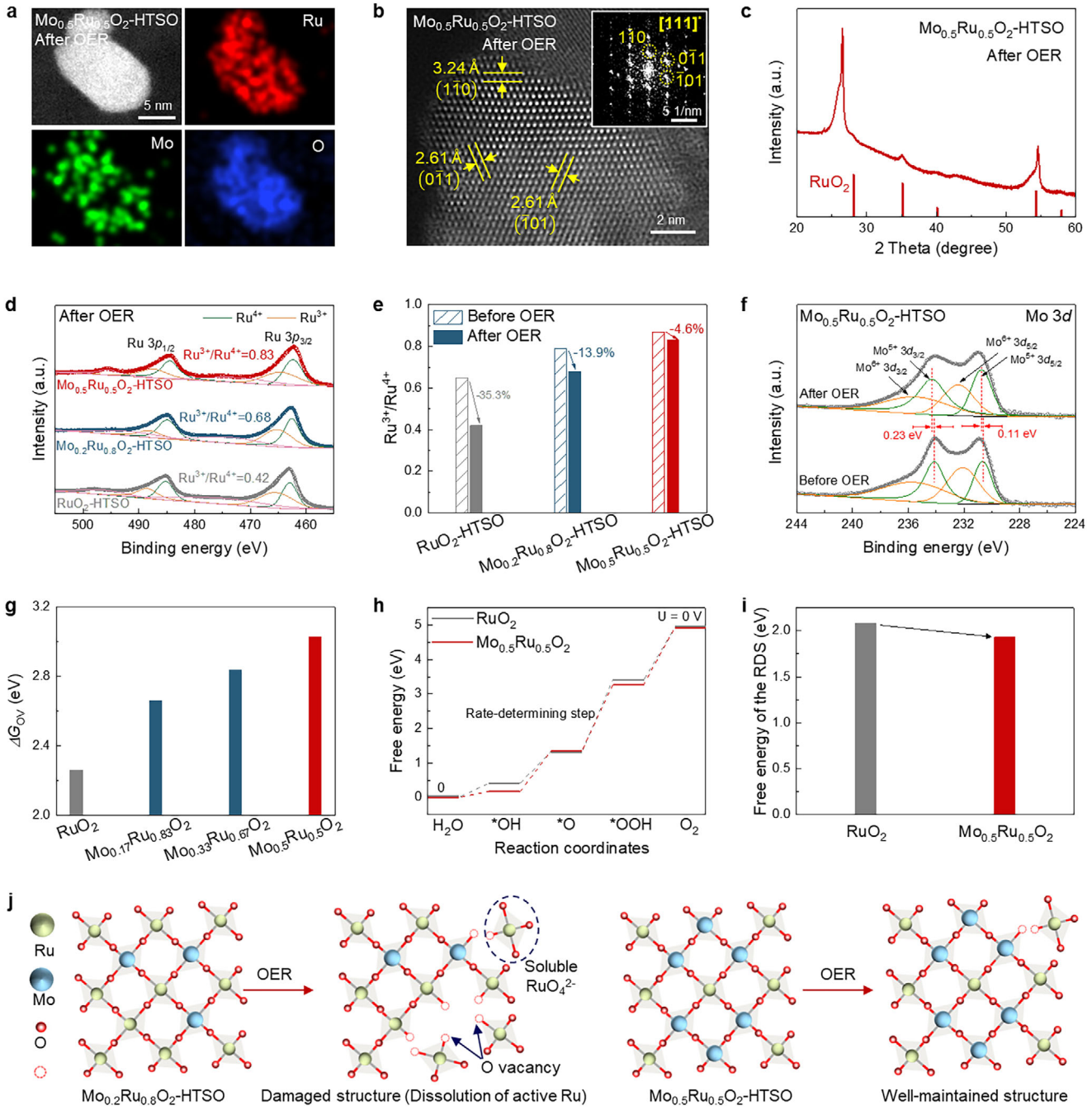

Figure 4. Post-OER analyses of $Mo_{0.5}Ru_{0.5}O_2$ and stability mechanism. a) TEM elemental maps of Mo, Ru, and O in $Mo_{0.5}Ru_{0.5}O_2$-HTSO after the 300-h OER stability test, indicating homogeneous elemental distribution; b) Atomic-resolution structure and corresponding FFT pattern of $Mo_{0.5}Ru_{0.5}O_2$-HTSO after the 300-h OER stability test, revealing a single-phase tetragonal structure; c) XRD patterns of $Mo_{0.5}Ru_{0.5}O_2$-HTSO before and after the 300-h OER stability test; d,e) XPS of (d) Ru *3p* spectra and (e) Ru^{3+}/Ru^{4+} ratio for RuO_2-HTSO, $Mo_{0.2}Ru_{0.8}O_2$-HTSO, and $Mo_{0.5}Ru_{0.5}O_2$-HTSO after the stability test; f) XPS spectra of Mo *3d* for $Mo_{0.5}Ru_{0.5}O_2$-HTSO before and after OER stability test; g) The calculated oxygen vacancy formation energies for different compositions of RuO_2, $Mo_{0.17}Ru_{0.83}O_2$, $Mo_{0.33}Ru_{0.67}O_2$, and $Mo_{0.5}Ru_{0.5}O_2$; h,i) (h) Four-step DFT free energy calculations and (i) free energies of the rate-determining step (RDS) for RuO_2 and $Mo_{0.5}Ru_{0.5}O_2$ for the OER; j) Schematic diagram of enhanced stability caused by higher Mo doping into RuO_2.

their OER performance (Figures S9 and S24, Supporting Information). The results indicate that the most effective dopants (such as Mo) should possess multiple accessible high oxidation states (e.g., 4^+–6^+) and ionic radii close to that of Ru^{4+} (0.62 Å). These characteristics enable stable substitution into the RuO_2 lattice while providing electronic flexibility for enhanced electron transfer to Ru, thereby improving both OER activity and stability.

3. Conclusion

This study presents a high-temperature thermal shock synthesis under an oxygen atmosphere (HTSO) for fabricating single-phase $Mo_{0.5}Ru_{0.5}O_2$ nanoparticles with enhanced stability and activity for the oxygen evolution reaction (OER) in acidic media. By rapidly heating precursor materials to ≈1200 °C for ≈0.05 s in oxygen, followed by swift quenching, we successfully circumvented the thermodynamic constraints that typically result in phase separation during conventional synthesis. The synthesized $Mo_{0.5}Ru_{0.5}O_2$ nanoparticles, ≈10 nm in size, exhibit a homogeneous tetragonal-like phase and demonstrate excellent electrochemical performance, including an overpotential of 210 mV at 10 mA cm^{-2} and sustained activity over 300 h at 50 mA cm^{-2}. Notably, while lower levels of metal doping (e.g., 20 at%) in RuO_2 have demonstrated only modest improvements in stability and are often accompanied by dopant dissolution and structural degradation, our results indicate that heavy Mo doping substantially reinforces the RuO_2 framework, resulting in markedly enhanced stability under OER conditions. These findings underscore the potential of HTSO as a versatile and effective strategy for developing robust, high-performance OER catalysts. Furthermore, the methodology's adaptability suggests its applicability to other dopants, co-doping, and high-entropy strategies for RuO_2-based systems, offering a promising avenue for the design of cost-effective and durable catalysts essential for the OER.

4. Experimental Section

Chemicals and Materials: Citric acid (99.5%), ruthenium chloride hydrate ($RuCl_3{\cdot}3H_2O$, 99.9%), and molybdenum(V) chloride ($MoCl_5$, 99.99%) were all purchased from Sigma–Aldrich. 2-propanol (99.9%), ethanol (99.9%), and 5 wt.% Nafion solution, perchloric acid ($HClO_4$, 70%) were purchased from Sigma–Aldrich. The carbon fiber paper (AvCarb MGL190) was purchased from FuelCell Store. 98% H_2SO_4 was purchased from Beijing Chemical Works. Gases including air and oxygen were purchased from Airgas. All chemicals were used as received without any further purification. All aqueous solutions were prepared using deionized water with a resistivity of 18.2 MΩ cm^{-1}.

Sol–Gel (SG) Synthesis of Mo-Doped RuO_2 Nanoparticles: In a typical process of $Mo_{0.2}Ru_{0.8}O_2$ synthesis, 0.1 mmol of citric acid, 0.01 mmol of $MoCl_5$, and 0.04 mmol of $RuCl_3{\cdot}3H_2O$ were dissolved in 10 mL DI water. The resulting homogenous solution was then sonicated for 30 min. Then, the solution was transferred to the muffle furnace and kept at 90 °C for 36 h. Next, the powder precursor was obtained, and it was transferred to the alumina boat and annealed in a muffle furnace at 600 °C for 1 h under an air atmosphere at a ramp rate of 10 °C min^{-1}. The resultant black product was collected and labeled as $Mo_{0.2}Ru_{0.8}O_2$-SG. Home-made RuO_2-SG, $Mo_{0.5}Ru_{0.5}O_2$-SG were prepared by the same synthetic procedure with different Ru/Mo feeding ratios.

High-Temperature Thermal Shock Synthesis of Mo-Doped RuO_2 Nanoparticles: Typically, individual metal salts ($MoCl_5$ and $RuCl_3{\cdot}3H_2O$) were dissolved in ethanol at designed ratios corresponding to $Mo_xRu_{1-x}O_2$ (x = 0.0, 0.2, 0.5, 0.6, and 1.0). The salt precursor solution was drop-cast onto carbon paper films to achieve an oxide mass loading of 0.5 mg cm^{-2} after heating. The samples were then dried at room temperature. The carbon paper films (4 cm in length × 1 cm in width) were clamped between two graphite plates on either side. The heating setup was placed in a home-built chamber, which could be filled with different atmospheres such as air or oxygen. The high-temperature thermal shock process was carried out via Joule heating of the precursor-loaded carbon paper films. The input signal was delivered from a source meter (2425, Keithley Source Meter) to a solid-state relay device (SSRDC150VDC25, Omega), allowing programmable control of the heating profile. The output signal from the solid-state relay was applied to the power source (MP10050D, Star Power) and the carbon paper film, connected in series. Different temperatures were achieved by tuning the voltage applied to the carbon paper film, thereby inducing oxide formation. A 0.05-s electrical pulse was used to synthesize the oxide nanoparticles of $Mo_xRu_{1-x}O_2$.

Characterizations and Measurements: Scanning electron microscope (SEM) images were acquired using a Hitachi SU8230 cold field emission SEM at 10 kV. For SEM characterization, Mo-doped RuO_2 distributed on carbon paper was affixed to the sample stage using double-sided conductive carbon tape (Oxford Instruments) to ensure proper adhesion and electrical conductivity. High-angle annular dark-field scanning transmission electron microscope (HAADF-STEM) images were captured with a Thermo Fisher Scientific Titan Themis 80–300 aberration-corrected S/TEM at 300 kV. This Themis S/TEM was equipped with an extreme field emission gun (X-FEG) and a DCOR+ probe Cs aberration corrector. The HAADF-STEM images were post-processed using DigitalMicrograph software (Gatan, Inc.). To reduce image noise, the lattice contrast of the HAADF-STEM images was enhanced using Gaussian smoothing and band-pass filter methods. Energy-dispersive X-ray spectroscopy (EDS) mappings were acquired with a Super-X detector (comprising four silicon drift detectors) at 300 kV. For TEM characterization, the sample was ground and ultrasonically dispersed in ethanol. A drop of the resulting suspension was deposited onto a copper TEM grid (Oxford Instruments) and dried at room temperature prior to measurement. An infrared camera (VarioCAM HDx head 600, 7.5–14 µm) with a resolution of 640 × 480 IR pixels and an image acquisition rate of 30 Hz was used to capture the temperature mapping of the Joule-heated carbon paper. The camera was positioned 20 cm away from the heating setup during measurement. ImageJ software was used to determine the particle size and size distribution of the nanoparticles. X-ray diffraction (XRD) patterns of the metal-doped RuO_2 samples were recorded on an X-ray diffractometer (Rigaku D/max 2500) with Cu $K\alpha$ radiation (40 kV, 30 mA) at a scan rate of 4° min^{-1}. XPS measurements were performed using a Nexsa Thermo Fisher Scientific spectrometer, using focused Al Kα monochromatic X-ray source (1486.6 eV) operated at 72 W and a high-resolution spherical mirror analyzer using 50 eV pass energy. The data acquisition was carried out using a 300 µm diameter X-ray beam and emitted photoelectrons were collected at the analyzer entrance slit normal to the sample surface. The chamber pressure was maintained at ≈ 5×10^{-9} Torr during the measurements. The dissolution of catalysts during the OER process at 1.65 V_{RHE} in a total volume of 100 mL electrolyte was quantified by ICP-MS (8900 Triple Quadrupole ICP-MS (Agilent Technologies, Inc.). A volume (5 mL) of electrolyte was used to fulfill the limit of detection of the equipment. The electrolyte for the as-prepared sample was sampled after 24 h electrolysis.

Electrochemical Measurements: Electrochemical measurements were performed using an electrochemical workstation (model CHI760D, CH Instruments) with a standard three-electrode electrochemical cell. The catalytic activity of samples was recorded in 0.1 M $HClO_4$ solution using the as-prepared or commercial samples, a plain graphite rod, and Ag/AgCl (saturated KCl) as the working, counter, and reference electrodes, respectively. All potentials in this study were calibrated to the reversible hydrogen electrode (RHE) using the Ag/AgCl reference electrode in 0.1 M $HClO_4$ electrolyte according to the following equation: $E_{RHE} = E_{Ag/AgCl} + 0.197\ V + 0.059\ V \times pH$. For the working electrode, a certain amount of the prepared catalysts (5 mg) and Nafion solution (5%, 10 µL) were dispersed in DI water (200 µL) and 2-propanol (800 µL) under ultrasonic conditions to obtain a homogenous catalyst ink. Then, the above suspension was

sprayed onto a carbon paper (CP) electrode (1 cm × 2.5 cm) and dried for further investigating the OER performance. The mass loading of catalysts is calculated as ≈0.5 mg cm^{-2}.

The LSV curves of electrocatalysts were then measured by scanning LSV from 1.1 to 1.7 V vs RHE in 0.1 M $HClO_4$ at a scan rate of 10 mV s^{-1} after the signals were stabilized via several CV scans. The accelerated stability CV tests (ADTs) were determined to screen the stability of catalysts by applying cyclic potential sweeps between 1.3 and 1.7 V vs RHE at a sweep rate of 50 mV s^{-1} for 4000 cycles. The CP tests were carried out at a current density of 50 mA cm^{-2}. The CA tests were conducted at 1.65 V_{RHE} for 24 h. During the durability test, the electrolyte was refreshed every 24 h to minimize pH variation and prevent contamination. Nyquist plots of Electrochemical impedance spectroscopy (EIS) measurements were collected in the frequency range of 0.01 Hz–1 MHz at 1.4 V_{RHE} electrode.

Calculation of Decay: The decay of as-prepared samples and reference catalysts was calculated by dividing the decay amount in CP by time. Then, the log10 decay value was shown.

Mass Activity: The mass activity (J_{mass}) of the samples was determined using the following equation:

$$J_{mass} = \frac{i_{geo}}{m_{cat} \times \mathrm{Ru}\ wt\%} \quad (1)$$

where i_{geo} is the geometric current (A) obtained from LSV, m_{cat} is the loading of catalysts on the electrode, and Ru wt.% is the mass ratio of Ru in $Mo_xRu_{1-x}O_2$, which is calculated from the results of ICP-MS.

TOF: The turnover frequency (TOF) values are determined using the following equation, under the assumption that all Ru ions in the catalysts are catalytically active and participate in the reaction.

$$TOF = \frac{Total\ hydrogen\ turnovers\ per\ geometric\ area}{active\ sites\ per\ geometric\ area} \quad (2)$$

The overall hydrogen turnover count was derived from the current density using the following equations:

Total hydrogen turnovers:

$$= \left[J\left(mA\,cm^{-2}\right)\right]\left[\frac{1\left(C\,s^{-1}\right)}{10^3\ (mA)}\right]\left[\frac{1\ \left(mol\,e^{-1}\right)}{96485\ (C)}\right]\left[\frac{1\,mol\,O_2}{4\,mol\,e^{-1}}\right]$$

$$\left[\frac{6.02\ \times\ 10^{23}\,molecules\,O_2}{1\,mol\,O_2}\right] = 1.56 \times 10^{15} H_2\,s^{-1}\,cm^{-2}\,per\,mA\,cm^{-2} \quad (3)$$

The number of active sites in $Mo_{0.5}Ru_{0.5}O_2$ was estimated from the total Ru mass on the electrode and the atomic weight of Ru:

$$= \left[\frac{1 \times 10^{-3} g\,cm^{-2} \times 0.375 wt\%}{101.07\,g\,mol^{-1}}\right]\left[\frac{6.02 \times 10^{22}}{1\ (mol\ Ru)}\right] = 2.23 \times 10^{17}\,Ru\ sites\,cm^{-2} \quad (4)$$

The current density obtained from the LSV curve are converted into TOF values according to:

$$TOF = \left[\frac{1.56 \times 10^{15}}{2.24 \times 10^{17}}\right] \times |j| = 0.007 \times |j|\ \left(s^{-1}\right) \quad (5)$$

Computational Details: The calculations of oxygen vacancy energies were performed by the density functional theory (DFT), as implemented in the Vienna ab initio simulation package (VASP). The Perdew–Burke–Ernzerhof (PBE) functional was used among the generalized gradient approximations (GGAs).[48] Electron-ion interactions were described by the projector-augmented wave (PAW) pseudopotentials with a cutoff energy of 400 eV.[49] The Ru_pv and Mo_sv potentials were used for Ru and Mo. The standard potential was chosen for O element. The exchange-correlation functional with a Gaussian smearing width term of 0.1 eV was used, and the convergence criteria for the energy and force were set to 1×10^{-5} eV and 0.03 eV $Å^{-1}$, respectively. The dipole moment correction was applied for the calculations of the slab model. Various doping Mo ratios ranging from 0.17 to 0.5 were investigated. For the surface, the RuO_2 (110) facet was selected. The slab model includes six layers, and the bottom two layers were fixed. The 5 × 3 × 1 Monkhorst-Pack grid k-points mesh was applied. The thickness of vacuum layer is 15 Å. Spin polarization effects were not considered in the current simulations, as the study focused on relative energy differences. In the density of states (DOS) calculations, the *k*-point smearing was treated using the tetrahedron method with Blöchl corrections. Three types of vacancies, i.e., O_{cus}, O_{bridge} and $O_{lattice}$ were studied. The oxygen vacancy formation free energies were calculated by the following equation.[50,51]

$$\Delta G = G_{vacancy} + G_O - G_{novacancy} \quad (6)$$

where $G_{vacancy}$ and $G_{novacancy}$ are the energies of the slabs with and without defects, respectively, and G_O is the chemical potential of oxygen (O), defined as half the total energy of an O_2 molecule. The VASPKIT software[52] was used to post-process the VASP simulation data.

Supporting Information

Supporting Information is available from the Wiley Online Library or from the author.

Acknowledgements

This project was not directly funded. The exploration of doping RuO_2 was financially supported by Energy Storage Materials Initiative (ESMI), which is a Laboratory Directed Research and Development Program at Pacific Northwest National Laboratory (PNNL). PNNL is operated by Battelle for the U.S. Department of Energy (DOE) under contract No. DE-AC05-76RLO1830. The TEM studies were performed using the facilities at the University of Connecticut (UConn)/Thermo Fisher Scientific Center for Advanced Microscopy and Materials Analysis (CAMMA). S.H. acknowledges the financial support provided by the Division of Chemical Sciences, Geosciences and Biosciences, Office of Basic Energy Sciences, of the U.S. Department of Energy through an Early Career grant No. DE-SC0021953.

Conflict of Interest

The authors declare no conflict of interest.

Author Contributions

K.Z., I.G.K. and F.L. contributed equally to this work. L.H., Y.S., and K.Z. designed the $Mo_xRu_{1-x}O_2$ system for the oxygen evolution reaction (OER) and developed the thermal shock synthesis method. K.Z. carried out the high-temperature thermal shock synthesis, as well as XRD, SEM, and temperature measurements. F.L. carried out high-resolution electron microscopy. P.G. calculated the formation free energy of oxygen vacancies. L.Y. supervised the work at PNNL and guided the doping strategy. I.K. performed the electrochemical measurements and data analyses. B.M.S. performed XPS measurements. T.W.W. conducted ICP measurements. Y.D. and Y.H. performed the XRD tests, while Q.Z. conducted the SEM characterization. C.Y. performed temperature measurements during Joule heating. K.Z., I.K., L.Y., T.L., and S.H. analyzed and discussed experimental results. K.Z. and I.K. co-wrote the manuscript with input from all authors. All authors reviewed and commented on the final manuscript.

Data Availability Statement

The data that support the findings of this study are available from the corresponding author upon reasonable request.

Keywords

catalysts, high-temperature thermal shock in oxygen, oxygen evolution reaction, single-phase $Mo_{0.5}Ru_{0.5}O_2$, stability

Received: October 14, 2025
Revised: November 12, 2025
Published online:

[1] L. C. Seitz, C. F. Dickens, K. Nishio, Y. Hikita, J. Montoya, A. Doyle, C. Kirk, A. Vojvodic, H. Y. Hwang, J. K. Norskov, T. F. Jaramillo, *Science* **2016**, *353*, 1011.
[2] A. Grimaud, A. Demortiere, M. Saubanere, W. Dachraoui, M. Duchamp, M. L. Doublet, J. M. Tarascon, *Nat. Energy* **2017**, *2*, 16189.
[3] Z. W. She, J. Kibsgaard, C. F. Dickens, I. Chorkendorff, J. K. Nørskov, T. F. Jaramillo, *Science* **2017**, *355*, aad4998.
[4] Y. Lee, J. Suntivich, K. J. May, E. E. Perry, Y. Shao-Horn, *J. Phys. Chem. Lett.* **2012**, *3*, 399.
[5] I. Roger, M. A. Shipman, M. D. Symes, *Nat. Rev. Chem.* **2017**, *1*, 0003.
[6] X. Wang, W. Pi, Z. Li, S. Hu, H. Bao, W. Xu, N. Yao, *Nat. Commun.* **2025**, *16*, 4845.
[7] F. Y. Chen, Z. Y. Wu, Z. Adler, H. Wang, *Joule* **2021**, *5*, 1704.
[8] K. Beppu, K. Obigane, F. Amano, *Catal. Sci. Tech.* **2023**, *13*, 6653.
[9] J. Zhang, X. Fu, S. Kwon, K. Chen, X. Liu, J. Yang, H. Sun, Y. Wang, T. Uchiyama, Y. Uchimoto, S. Li, Y. Li, X. Fan, G. Chen, F. Xia, J. Wu, Y. Li, Q. Yue, L. Qiao, D. Su, H. Zhou, W. A. Goddard, Y. Kang, *Science* **2025**, *387*, 48.
[10] S. Cherevko, A. R. Zeradjanin, A. A. Topalov, N. Kulyk, I. Katsounaros, K. J. J. Mayrhofer, *Chem. Cat. Chem.* **2014**, *6*, 2219.
[11] X. Ping, Y. Liu, L. Zheng, Y. Song, L. Guo, S. Chen, Z. Wei, *Nat. Commun.* **2024**, *15*, 2501.
[12] D. Y. Chung, P. P. Lopes, P. Farinazzo Bergamo Dias Martins, H. He, T. Kawaguchi, P. Zapol, H. You, D. Tripkovic, D. Strmcnik, Y. Zhu, S. Seifert, S. Lee, V. R. Stamenkovic, N. M. Markovic, *Nat. Energy* **2020**, *5*, 222.
[13] S. Z. Oener, A. Bergmann, B. R. Cuenya, *Nat. Synth.* **2023**, *2*, 817.
[14] Q. Lu, J. Liu, X. Zou, B. Huang, W. Wu, J. Yin, Z. Q. Liu, Y. Wang, *Angew. Chem. Int. Ed.* **2025**, *64*, 202503733.
[15] C. Rong, K. Dastafkan, Y. Wang, C. Zhao, *Adv. Mater.* **2023**, *35*, 2211884.
[16] J. He, W. Li, P. Xu, J. Sun, *Appl. Catal. B: Environ.* **2021**, *298*, 120528.
[17] Y. Wang, X. Wen, X. Dong, C. Xu, W. Ma, Y. Sun, B. Xu, C. Li, *Cryst. Eng. Comm.* **2023**, *25*, 4480.
[18] Y. Zhang, J. Dong, T. Sun, X. Zhang, J. Chen, L. Xu, *Small* **2024**, *20*, 2305889.
[19] Y. Wang, Y. Wen, Y. Cheng, X. Chen, M. Zhuansun, T. Wang, J. Li, D. Meira, H. Sun, J. Wei, J. Zhou, Y. Wang, S. He, *Nano Res.* **2024**, *17*, 1165.
[20] J. L. Cai, J. Y. Fan, X. D. Zhang, X. Xie, W. Y. Tian, X. G. Zhang, J. Ding, Y. S. Liu, *Rare Met.* **2024**, *43*, 5095.
[21] C. Li, J. Chen, K. C. Chong, L. Wang, B. Liu, *Small Struct.* **2024**, *5*, 2300394.
[22] F. A. Cotton, J. T. Mague, *Inorg. Chem.* **1966**, *5*, 317.
[23] D. O. Scanlon, G. W. Watson, D. J. Payne, G. R. Atkinson, R. G. Egdell, D. S. L. Law, *J. Phys. Chem. C* **2010**, *114*, 4636.
[24] N. J. Stedman, A. K. Cheethamb, P. D. Battle, *J. Mater. Chem.* **1994**, *4*, 641.
[25] C. Zhu, H. Xin, J. Hong, H. Wang, C. Wang, L. Ma, Q. Liu, *ACS Sustain. Chem. Eng.* **2021**, *9*, 14704.
[26] W. Lv, X. Hu, Y. Zhu, Y. Xu, S. Liu, P. Chen, C. Wang, L. Ma, *Ren. Energy* **2022**, *188*, 195.
[27] Y. Yao, Z. Huang, P. Xie, S. D. Lacey, R. J. Jacob, H. Xie, F. Chen, A. Nie, T. Pu, M. Rehwoldt, D. Yu, M. R. Zachariah, C. Wang, R. Shahbazian-Yassar, J. Li, L. Hu, *Science* **2018**, *359*, 1489.
[28] Y. Yao, Q. Dong, A. Brozena, J. Luo, J. Miao, M. Chi, C. Wang, I. G. Kevrekidis, Z. J. Ren, J. Greeley, G. Wang, A. Anapolsky, L. Hu, *Science* **2022**, *376*, abn3103.
[29] S. Fjellvåg, A. Ruud, H. H. Sønsteby, O. Nilsen, H. Fjellvåg, *Crys. Growth Des.* **2020**, *20*, 3861.
[30] T. Li, Y. Yao, Z. Huang, P. Xie, Z. Liu, M. Yang, J. Gao, K. Zeng, A. H. Brozena, G. Pastel, M. Jiao, Q. Dong, J. Dai, S. Li, H. Zong, M. Chi, J. Luo, Y. Mo, G. Wang, C. Wang, R. Shahbazian-Yassar, L. Hu, *Nat. Catal.* **2021**, *4*, 62.
[31] S. Hao, M. Liu, J. Pan, X. Liu, X. Tan, N. Xu, Y. He, L. Lei, X. Zhang, *Nat. Commun.* **2020**, *11*, 5368.
[32] H. Liu, Z. Zhang, J. Fang, M. Li, M. G. Sendeku, X. Wang, H. Wu, Y. Li, J. Ge, Z. Zhuang, D. Zhou, Y. Kuang, X. Sun, *Joule* **2023**, *7*, 558.
[33] H. Jin, X. Liu, P. An, C. Tang, H. Yu, Q. Zhang, H. J. Peng, L. Gu, Y. Zheng, T. Song, K. Davey, U. Paik, J. Dong, S. Z. Qiao, *Nat. Commun.* **2023**, *14*, 354.
[34] Z. Li, S. Wang, Y. Tian, B. Li, H. J. Yan, S. Zhang, Z. Liu, Q. Zhang, Y. Lin, L. Chen, *Chem. Commun.* **2020**, *56*, 1749.
[35] Y. Lin, Z. Tian, L. Zhang, J. Ma, Z. Jiang, B. J. Deibert, R. Ge, L. Chen, *Nat. Commun.* **2019**, *10*, 162.
[36] S. Chen, H. Huang, P. Jiang, K. Yang, J. Diao, S. Gong, S. Liu, M. Huang, H. Wang, Q. Chen, *ACS Catal.* **2020**, *10*, 1152.
[37] Y. Tian, S. Wang, E. Velasco, Y. Yang, L. Cao, L. Zhang, X. Li, Y. Lin, Q. Zhang, L. Chen, *iScience* **2020**, *23*, 100756.
[38] Z. Y. Wu, F. Y. Chen, B. Li, S. W. Yu, Y. Z. Finfrock, D. M. Meira, Q. Q. Yan, P. Zhu, M. X. Chen, T. W. Song, Z. Yin, H. W. Liang, S. Zhang, G. Wang, H. Wang, *Nat. Mater.* **2023**, *22*, 100.
[39] J. Su, R. Ge, K. Jiang, Y. Dong, F. Hao, Z. Tian, G. Chen, L. Chen, *Adv. Mater.* **2018**, *30*, 1801351.
[40] D. Zhang, M. Li, X. Yong, H. Song, G. I. N. Waterhouse, Y. Yi, B. Xue, D. Zhang, B. Liu, S. Lu, *Nat. Commun.* **2023**, *14*, 2517.
[41] Y. Zi, C. Zhang, J. Zhao, Y. Cheng, J. Yuan, J. Hu, *Small* **2024**, *20*, 2406657.
[42] Y. Wang, R. Yang, Y. Ding, B. Zhang, H. Li, B. Bai, M. Li, Y. Cui, J. Xiao, Z. S. Wu, *Nat. Commun.* **2023**, *14*, 1412.
[43] Z. Shi, J. Li, Y. Wang, S. Liu, J. Zhu, J. Yang, X. Wang, J. Ni, Z. Jiang, L. Zhang, Y. Wang, C. Liu, W. Xing, J. Ge, *Nat. Commun.* **2023**, *14*, 843.
[44] L. Li, G. Zhang, J. Xu, H. He, B. Wang, Z. Yang, S. Yang, *Adv. Funct. Mater.* **2023**, *33*, 2213304.
[45] L. Li, G. Zhang, C. Zhou, F. Lv, Y. Tan, Y. Han, H. Luo, D. Wang, Y. Liu, C. Shang, L. Zeng, Q. Huang, R. Zeng, N. Ye, M. Luo, S. Guo, *Nat. Commun.* **2024**, *15*, 4974.
[46] J. Tang, Q. Zeng, Q. Jiang, H. Wang, S. Hu, Y. Ji, H. Zeng, C. Liu, H. J. Peng, X. Li, T. Zheng, C. W. Pao, X. Liu, C. Xia, *Chem. Catal.* **2025**, *5*, 101441.
[47] B. Yuan, Q. Dang, H. Liu, M. G. Sendeku, J. Peng, Y. Fan, L. Cai, A. Cao, S. Chen, H. Li, Y. Kuang, F. Wang, X. Sun, *Nat. Commun.* **2025**, *16*, 4583.
[48] J. P. Perdew, K. Burke, M. Ernzerhof, *Phys. Rev. Lett.* **1996**, *77*, 3865.
[49] G. Kresse, D. Joubert, *Phys. Rev. B* **1999**, *59*, 1758.
[50] Y. Hinuma, T. Kamachi, N. Hamamoto, M. Takao, T. Toyao, K. I. Shimizu, *J. Phys. Chem. C* **2020**, *124*, 10509.
[51] Z. Wei, Y. Bao, Y. Wang, S. Li, *Catal. Sci. Tech.* **2025**, *15*, 1538.
[52] V. Wang, N. Xu, J. Liu, G. Tang, W. Geng, *Comp. Phys. Commun.* **2021**, *267*, 108033.